SAND2022-4296C

Proceedings of the ASME 2022
Pressure Vessels & Piping Conference
PVP 2022
July 17-22, 2022, Las Vegas, Nevada, USA

PVP2022-84797

INFLUENCE OF HIGH-PRESSURE HYDROGEN GAS AND PRE-CHARGED HYDROGEN ON FATIGUE CRACK INITIATION AND FATIGUE LIFE OF 255 SUPER DUPLEX STAINLESS STEEL

B. Kagay[1]
Materials Testing Institute
University of Stuttgart
Stuttgart, Germany

J. Ronevich
Sandia National Laboratories
Livermore, CA, USA

C. San Marchi
Sandia National Laboratories
Livermore, CA, USA

ABSTRACT

High strength austenite-ferrite duplex stainless steels are a potential alternative to austenitic stainless steels for components in hydrogen gas storage systems. Since these components experience cyclic loading from frequent pressurization and depressurization, the effect of hydrogen on the fatigue behavior of duplex stainless steel must be understood. To determine the influence of hydrogen on fatigue crack initiation and fatigue life of a 255 super duplex stainless steel, circumferentially notched tensile (CNT) specimens were fatigue tested in the as-received condition in air, with pre-charged internal hydrogen in air, and in the as-received condition in high pressure hydrogen gas. The direct current potential difference (DCPD) method was used to detect crack initiation so that S-N curves could be produced for both (i) cycles to crack initiation and (ii) cycles to failure. An electropolished CNT specimen was also cycled in the as-received and hydrogen pre-charged conditions but interrupted just after crack initiation. The microstructural locations of small fatigue cracks were then identified with scanning electron microscopy and electron backscatter diffraction (EBSD). High pressure hydrogen gas and pre-charged hydrogen decreased the fatigue life of 255 duplex stainless steel by a nearly identical amount. The effects of hydrogen on fatigue crack initiation and fatigue life of 255 duplex stainless steel are discussed and compared to austenitic stainless steels.

INTRODUCTION

As the utilization of gaseous hydrogen in the energy sector increases, alloys with a higher strength and/or lower cost than austenitic stainless steels are being considered for components in gas storage systems. High-strength duplex stainless steels (DSS) consisting of austenite islands in a ferrite matrix are one potential alternative. Duplex stainless steels have been shown to be susceptible to hydrogen embrittlement. The fracture toughness [1, 2] and tensile ductility [3] of duplex stainless steels is known to be decreased by internal hydrogen. External gaseous hydrogen has also been shown to decrease the fracture toughness [4] and increase the fatigue crack growth rate [5] of duplex stainless steels. Cleavage of the ferritic phase has been observed to occur when hydrogen is present, but the austenite phase is also considered to be critical for cracking processes with internal hydrogen [1] as well as during fatigue [6].

Fatigue performance in a hydrogen environment is critical to the implementation of an alloy in a gas storage system due to the cyclic stresses caused by pressure cycling. A greater understanding of the effect of hydrogen on fatigue life and fatigue crack initiation in duplex stainless steels and the role of the austenite and ferrite phases in the cracking processes would aid in the design and implementation of stainless steels in hydrogen gas storage systems.

In this study, the effects of internal and external hydrogen on the fatigue life of 255 duplex stainless steel is evaluated through fatigue testing of circumferentially notched tension (CNT) specimens. The direct current potential difference (DCPD) technique is also used to assess the cycles up to crack initiation and to interrupt tests when only small cracks have formed. For specimens with and without internal hydrogen the location of small cracks in the microstructure are determined with scanning electron microscopy and electron backscatter diffraction (EBSD). The influence of hydrogen on the fatigue life, cycles to crack initiation, and microstructural crack path are discussed and compared to austenitic stainless steels.

[1]Previously with Sandia National Laboratories

Sandia National Laboratories is a multimission laboratory managed and operated by National Technology & Engineering Solutions of Sandia, LLC, a wholly owned subsidiary of Honeywell International Inc., for the U.S. Department of Energy's National Nuclear Security Administration under contract DE-NA0003525.

EXPERIMENTAL PROCEDURES

255 super duplex stainless steel rolled bar with the composition shown in Table 1 was evaluated. The composition of a 316L bar from a previous study for which the fatigue results will be compared to the 255 DSS is also provided in Table 1 [7]. CNT and smooth tensile specimens were extracted from the 255 DSS bar with the tensile direction parallel to the rolling direction. The CNT specimens were machined with a major diameter of 5.7 mm (0.225"), a minimum diameter of 4.06 mm (0.160"), and a root radius of 0.127 mm (0.005"), which corresponds to a K_t of 3.9. Load-control tension-tension fatigue testing of the CNT specimens was performed at a frequency of 1 Hz and with an R-ratio of 0.1. Notched tensile testing of the CNT specimens was performed at a crosshead displacement rate of 8.5×10^{-5} mm·s^{-1} The cylindrical specimens used for tensile testing were machined with a gauge diameter of approximately 2.87 mm. Tensile testing was performed at a constant displacement rate corresponding to a strain rate of 1.7×10^{-3} s^{-1} and with a 12.7 mm (0.5 in) extensometer to measure elongation. All fatigue and tensile tests were performed on servohydraulic load frames.

Fatigue testing and notched tensile testing were performed on 255 DSS specimens for 3 environmental conditions: without internal hydrogen (as-received (AR)), with internal hydrogen (hydrogen pre-charged (PC)), and in high pressure 103 MPa hydrogen gas (HP). Tensile tests of smooth specimens were performed for the AR and PC conditions. The tests of the AR and PC specimens were performed in the ambient laboratory environment, and tests of all conditions were performed at a temperature of approximately 20°C. The PC specimens were thermally pre-charged in gaseous hydrogen at a pressure of 138 MPa and a temperature of 300°C for at least 10 days. The PC specimens were stored in a freezer at −50°C (223K) to prevent hydrogen egress after pre-charging. The hydrogen content of the PC DSS was 97 wt ppm., as measured by inert gas fusion.

The cycles to crack initiation was determined with the DCPD method. Two wires were spot-welded about 15 mm away from the notch on opposite sides of the specimen to provide a constant current of 1 A across the length of the specimen. Two wires to measure voltage were spot-welded 1 mm away from the notch on opposite sides of the specimen. The direction of current flow was reversed every 5 s to minimize thermoelectric effects. The number of cycles to crack initiation was selected as the inflection point at which the DCPD voltage signal began to continuously increase at an increasing rate.

The notches of one AR and one PC CNT specimen were electropolished prior to fatigue testing so that SEM imaging and EBSD could be performed after testing. The tests of the electropolished specimens were interrupted shortly after crack initiation was identified through the DCPD signal. Scanning electron imaging and EBSD was then performed on the notches of the CNT specimens with a FEI Helios Nanolab Dualbeam FIB/SEM. An accelerating voltage of 25 keV and step sizes between 0.05 μm and 0.2 μm were used for EBSD. The SEM images were captured with the Everhart-Thornley detector and were tilt-corrected.

RESULTS

The tensile properties of the 255 DSS bar for the as-received (AR) and hydrogen pre-charged (PC) conditions are shown in Table 2. The tensile properties of the strain-hardened 316L bar from the previous study are also provided in Table 2 for the same environmental conditions [7]. Pre-charged hydrogen increased the yield stress and ultimate tensile stress (UTS) and decreased the uniform elongation, total elongation, and reduction of area of the 255 DSS alloy. These effects of internal hydrogen on tensile properties of 255 DSS are similar to the effects of internal hydrogen on austenitic stainless steels. The notched tensile strength (NTS) determined from tensile testing of the 255 DSS CNT specimens is provided in Table 3 along with the values for the 316L bar. The PC and HP specimens exhibited a lower NTS than the AR specimens, and internal hydrogen (PC) and external hydrogen (HP) decreased the NTS by a similar amount. For the 316L bar, the PC condition exhibited the highest NTS, while the HP condition exhibited the lowest NTS.

Table 1 – Composition of 255 DSS Bar From This Study and 316L Bar From a Previous Study [7]

wt %	Cr	Ni	Mn	Mo	C	N	Si	S	P	Cu	Fe
255 DSS Bar	25.9	6.21	0.87	3.28	0.018	0.224	0.38	0.0007	0.024	1.56	Bal.
316L Bar	17.54	12.04	1.15	2.05	0.020	0.04	0.51	0.023	0.028		Bal.

Table 2 – Tensile Properties of As-Received (AR) and Hydrogen Pre-Charged (PC) 255 DSS Bar and 316L Bar

	Condition	0.2% Yield Stress (MPa)	UTS (MPa)	Uniform Elongation (%)	Total Elongation (%)	Reduction of Area (%)
255 DSS Bar	AR	708	852	22.1	46.4	81.7
255 DSS Bar	PC	833	924	14.5	20.1	22.8
316L Bar	AR	573	731	26.6	54.5	76.6
316L Bar	PC	648	793	27.1	47.6	60.2

Table 3 – Notched Tensile Strength of 255 DSS Bar and 316L Bar in the As-Received (AR), Hydrogen Pre-Charged (PC) and High Pressure Hydrogen (HP) Conditions

	Condition	Notched Tensile Strength (MPa)
255 DSS Bar	AR	1281
255 DSS Bar	PC	921
255 DSS Bar	HP	906
316L Bar	AR	1094
316L Bar	PC	1170
316L Bar	HP	1045

Fatigue life results for the 255 DSS alloy in the AR, PC, and HP conditions are plotted as maximum net-section stress (S_{max}) versus cycles to failure in Figure 1 (a). The filled symbols in Figure 1 (a) and all subsequent S-N plots in this document are tests that reached failure, while the open symbols are tests that were stopped prior to failure. As seen in the S-N curves in Figure 1 (a), the PC and HP conditions exhibit shorter fatigue lives and appear to reach a fatigue limit at a much lower stress than for the AR condition.

The data from Figure 1 (a) is re-plotted with the maximum applied stress normalized by the notched tensile strength (S_{max}/NTS) in Figure 1 (b). The AR, PC, and HP conditions all exhibit similar fatigue life and fatigue limit when the maximum stress is normalized by the NTS.

The cycles to crack initiation as measured by the DCPD method are plotted versus the maximum net-section stress (S_{max}) for the 255 DSS AR, PC, and HP conditions, as well as for a strain-hardened 316L bar tested in the same conditions, in Figure 2 (a). In Figure 2 (b) the cycles to crack initiation for 255 DSS and 316L are re-plotted versus the maximum applied stress normalized by the notched tensile strength (S_{max}/NTS).

The cycles to crack initiation data for 255 DSS in Figure 2 shows the same effect of hydrogen as for the cycles to failure data in Figure 1. The AR condition exhibits greater cycles to crack initiation than the PC and HP conditions versus the maximum applied stress in Figure 2 (a), but all three conditions show similar cycles to crack initiation when the maximum stress is normalized by the NTS as in Figure 2 (b).

For the 316L bar, the PC condition exhibits slightly greater cycles to crack initiation and the HP condition exhibits slightly lower cycles to crack initiation compared to the AR condition when plotted versus the maximum applied stress (Figure 2 (a)). The cycles to crack initiation versus maximum applied stress curves for the 316L AR, PC, and HP conditions are close to the curves for the 255 DSS PC and HP conditions, but fall below the curve for the 255 DSS AR condition.

The cycles to crack initiation data for the 316L bar also correspond when the maximum stress is normalized by the NTS as shown in Figure 2 (b). The 316L bar exhibits lower cycles to crack initiation than the 255 DSS bar for all three AR, PC, and HP conditions when plotted versus the maximum stress normalized by the NTS.

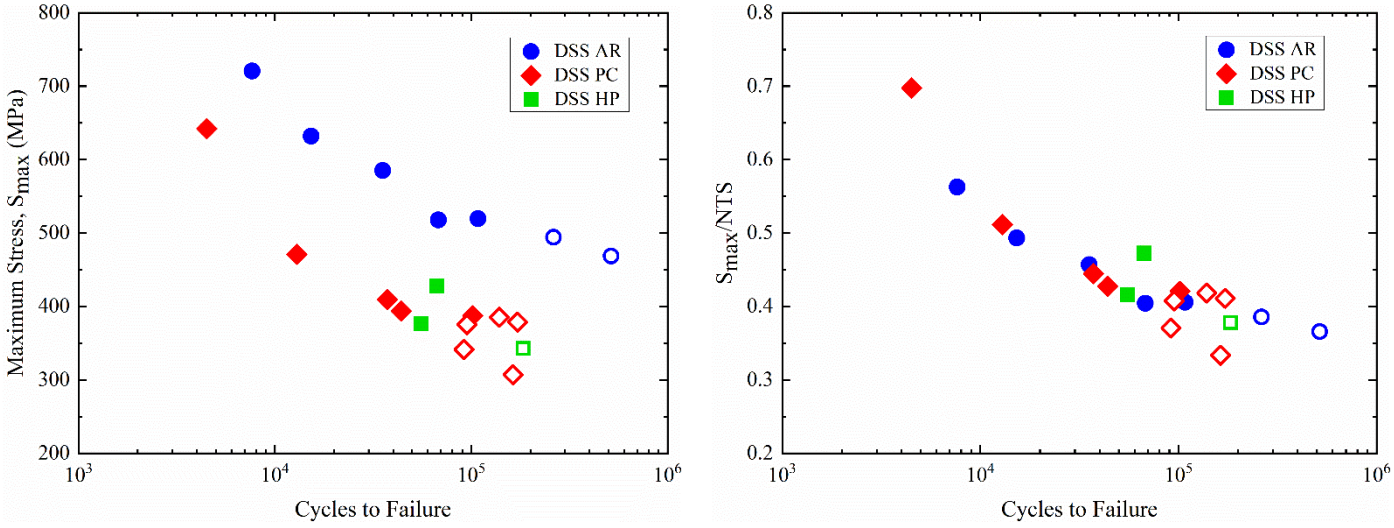

(a) **(b)**

Figure 1 Fatigue life of the 255 DSS bar in the AR, PC, and HP conditions plotted versus (a) maximum applied stress (S_{max}) and (b) maximum applied stress normalized by the notched tensile stress (S_{max}/NTS). The filled symbols are tests that reached failure, and the open symbols are tests that were stopped prior to failure.

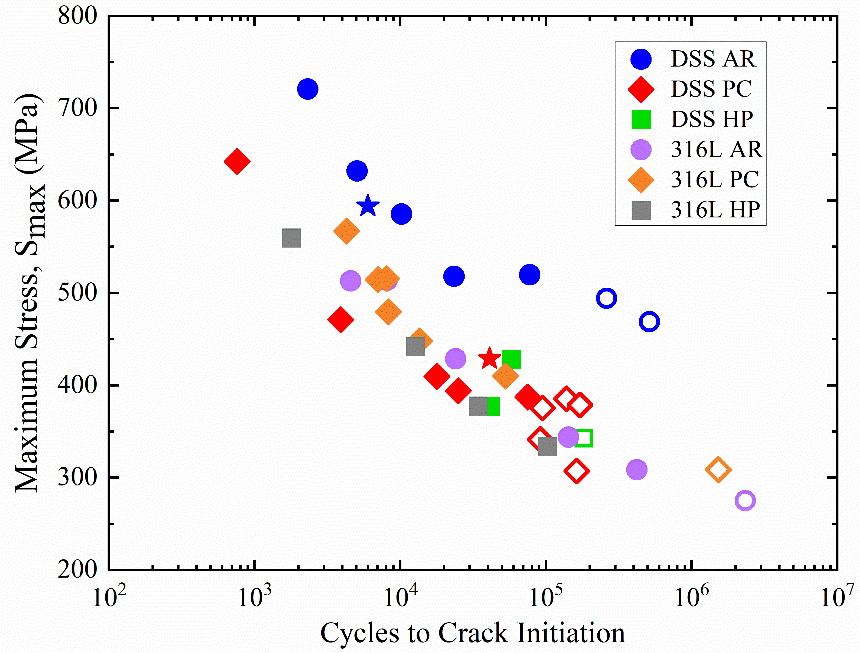

(a)

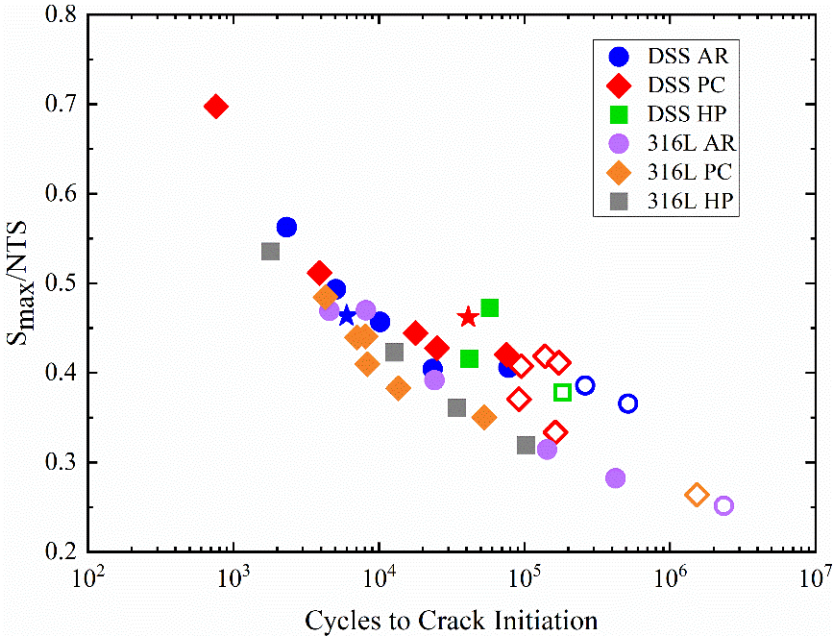

(b)

Figure 2 Cycles to crack initiation of the 255 DSS bar and a 316L bar in the AR, PC, and HP conditions plotted versus (a) maximum applied stress (S_{max}) and (b) maximum applied stress normalized by the notched tensile stress (S_{max}/NTS). The filled symbols are tests that reached failure, and the open symbols are tests that were stopped prior to failure. Star symbols indicate the tests that were interrupted for EBSD analysis.

The maximum applied cyclic stress (S_{max}), normalized maximum stress (S_{max}/NTS), and cycles to crack initiation determined with DCPD (N_i) for the interrupted tests of the AR and PC electropolished specimens are given in Table 4. The cycles to crack initiation for the interrupted tests are also plotted as stars in Figure 2. Crack initiation occurred at a greater number of cycles for the PC condition than the AR condition for these tests at the same normalized maximum stress, although the absolute stress for the AR condition was higher since the NTS of the PC condition is 30% lower compared to the AR condition.

Multiple cracks were observed in the notches of both the AR and PC 255 DSS CNT specimens from the interrupted tests. Examples of the cracks in the notches of the CNT specimens are shown in the (a) scanning electron micrographs, (b) phase maps, and (c) inverse pole figure (IPF) maps in Figures 3-6. For all images in Figures 3-6. the loading direction is horizontal, and the IPF map is for the horizontal direction. For the phase maps, austenite (γ) is red, and ferrite (α) is green.

Small cracks of less than 20 µm were only observed for the AR condition and are shown in Figure 3. These cracks in the AR condition intersect a γ/α phase boundary and propagate almost entirely across a single austenite island. The crack on the right also appears to slightly propagate into the ferrite grain.

In the AR condition cracks were observed to propagate along γ/α phase boundaries, α/α grain boundaries, γ/γ grain boundaries, and transgranularly through ferrite and austenite. A single crack in the 255 DSS AR specimen propagating along each of these locations is labeled in Figure 4. The transgranular cracks in both the austenite and ferrite in Figure 4 propagate parallel to slip traces and intrusions/extrusions.

For the PC condition, γ/α phase boundary cracking, transgranular cracking in ferrite and austenite, and cracking along twin boundaries in austenite was observed. Transgranular cracking in ferrite and austenite is visible for the 255 DSS PC condition in Figure 5. Transgranular cracks in the PC condition took two forms: cracks that ran parallel to slip traces as in the upper portion of the crack in Figure 5 and long cracks running perpendicular to the loading direction that extended through several grains as seen in the lower portion of the crack in Figure 5. Crack propagation along twin boundaries in the austenite can be seen in Figure 6. The crack in Figure 6 intersects an austenite island, in which the crack propagates in a transgranular manner up to the twin boundary, propagates along the twin boundary, and then propagates transgranularly again before exiting into the ferrite. The crack in Figure 6 also intersects a γ/γ/γ/α quadruple point.

Table 4 – S_{max}, S_{max}/NTS, and Cycles to Initiation (N_i) for Fatigue Tests of AR and PC Electropolished 255 DSS CNT Specimens

Condition	S_{max} (MPa)	S_{max} / NTS	N_i
AR	594	0.46	6,000
PC	429	0.46	41,100

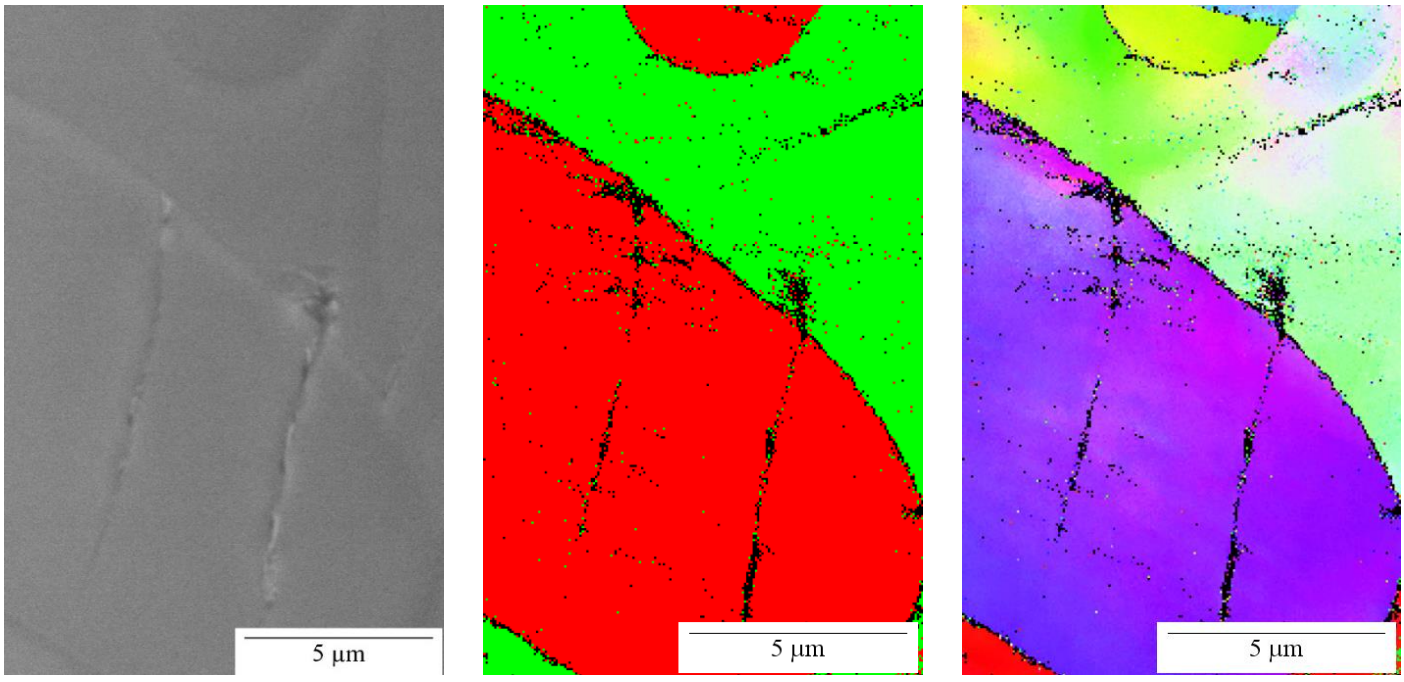

(a) **(b)** **(c)**

Figure 3 (a) Scanning electron micrograph, (b) phase map (austenite-γ = red, ferrite-α = green), and (c) IPF map of cracks in a 255 DSS AR CNT specimen. Loading direction is horizontal. IPF map for loading-direction. Step size of 0.05 µm.

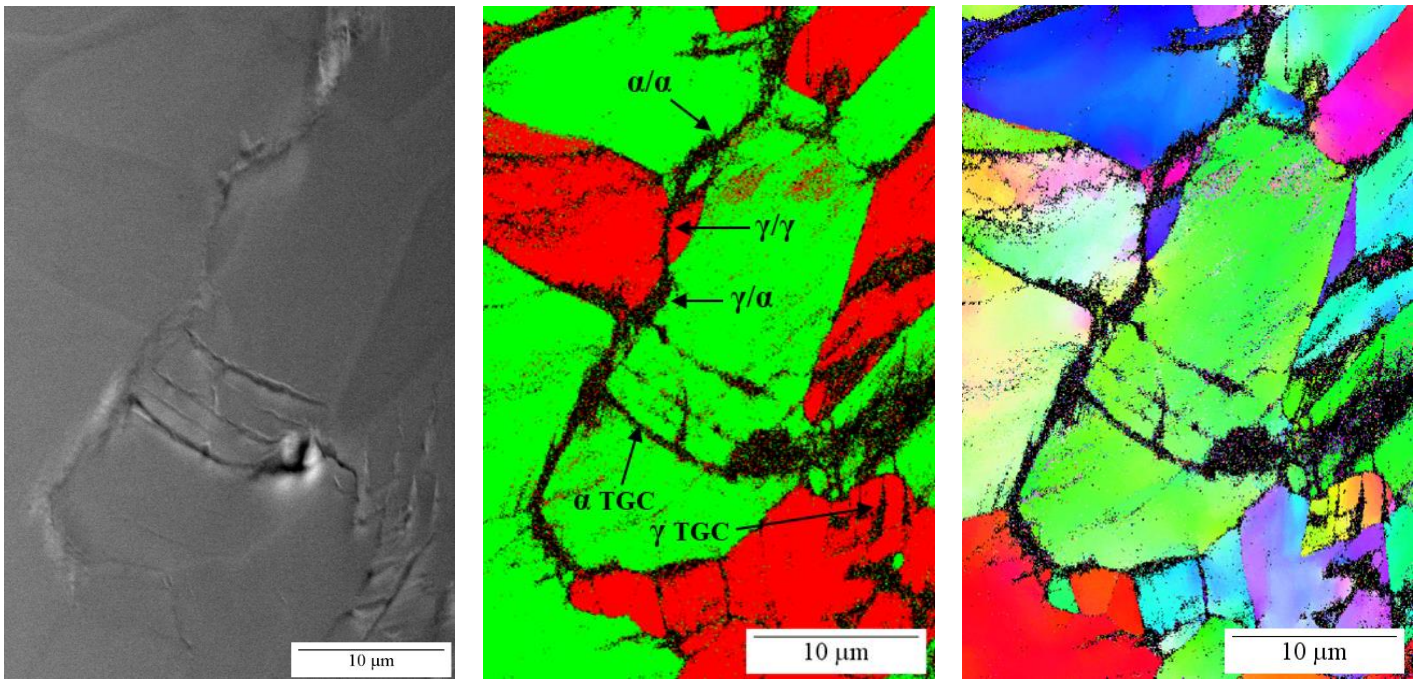

(a) **(b)** **(c)**

Figure 4 (a) Scanning electron micrograph, (b) phase map (austenite-γ = red, ferrite-α = green), and (c) IPF map of cracks in a 255 DSS AR CNT specimen. Loading direction is horizontal. IPF map for loading-direction. Step size of 0.05 µm.

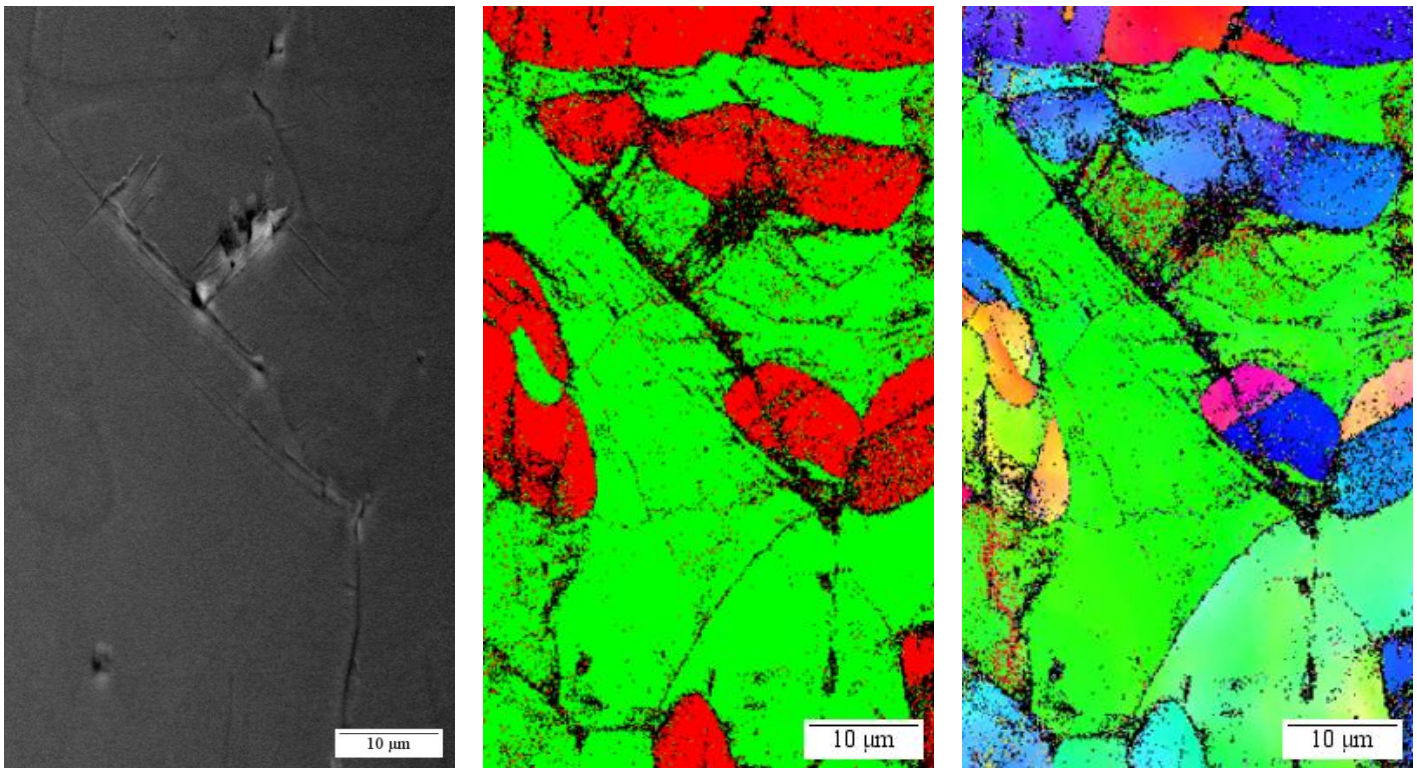

(a) **(b)** **(c)**

Figure 5 (a) Scanning electron micrograph, (b) phase map (austenite-γ = red, ferrite-α = green), and (c) IPF map of cracks in a 255 DSS PC CNT specimen. Loading direction is horizontal. IPF map for loading-direction. Step size of 0.16 µm.

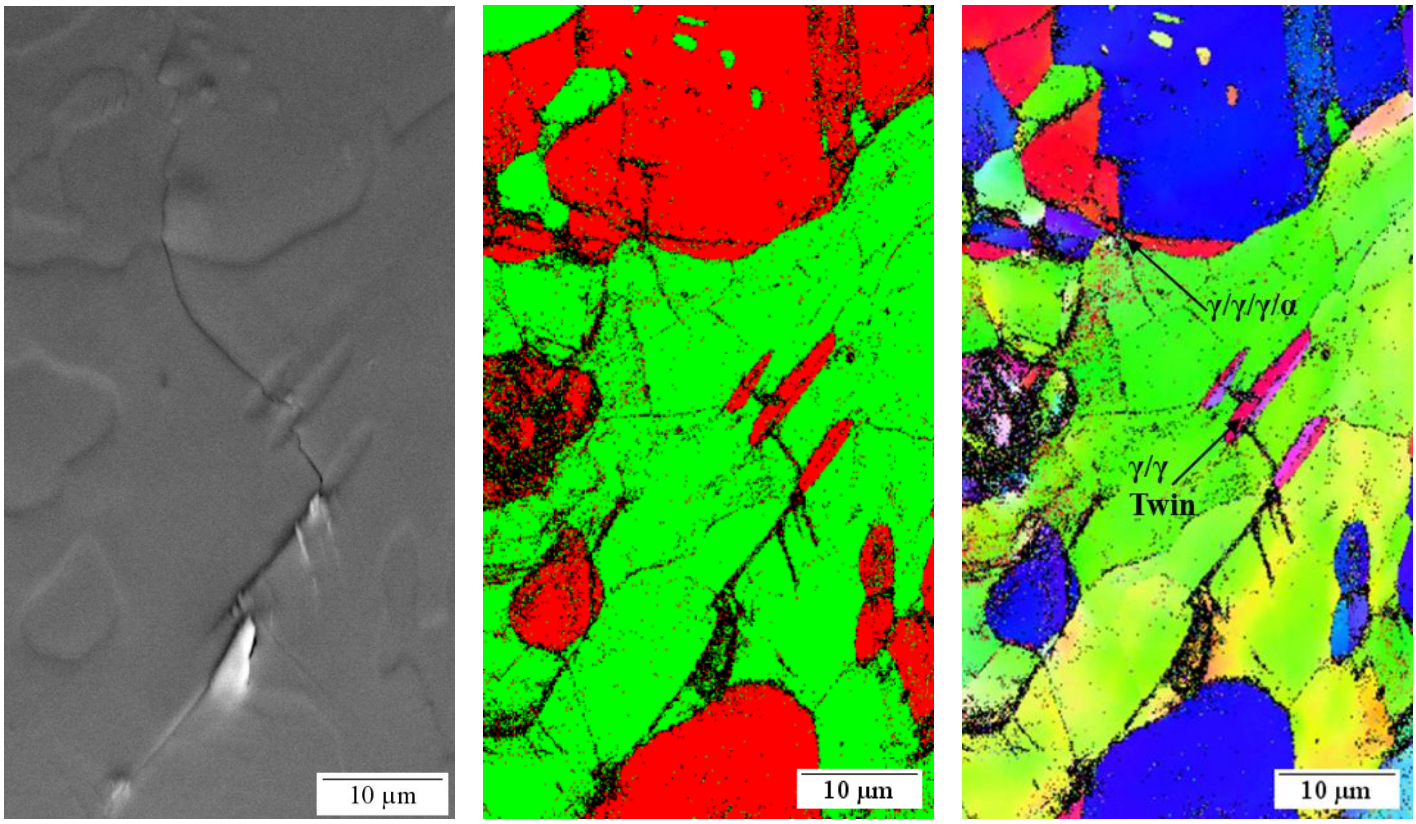

Figure 6 (a) Scanning electron micrograph, (b) phase map (austenite-γ = red, ferrite-α = green), and (c) IPF map of cracks in a 255 DSS PC CNT specimen. Loading direction is horizontal. IPF map for loading-direction. Step size of 0.13 µm.

DISCUSSION

Internal hydrogen (PC) and external hydrogen (HP) both decreased the fatigue life, fatigue limit, and cycles to crack initiation of 255 DSS by a similar degree. Since internal and external hydrogen also decreased the NTS by a similar amount, normalization of the applied stresses by the NTS caused the S-N curves for the AR, PC, and HP conditions to collapse into a narrow band.

Normalization of the applied stresses by a strength parameter (yield strength, UTS, etc.) can account for the influence of the material properties on the evolution of the stress and strain fields during fatigue [8-10]. The engineering UTS is frequently chosen for normalization of the maximum stresses because the UTS includes contributions from both the material's yield stress and strain hardening. Normalization by the UTS has been shown to collapse fatigue data for 316L with and without internal hydrogen [11], but normalization by the UTS does not collapse the fatigue data for 255 DSS. For 316L the fatigue lives are greater with internal hydrogen than without internal hydrogen, and normalization by the UTS captures the increase in flow strength due to internal hydrogen. For 255 DSS the fatigue lives are shorter with internal hydrogen than for the as-received material so normalization by the UTS does not collapse the S-N curves.

Normalization by the NTS collapses both the 255 DSS and 316L S-N_i curves. This observation indicates that normalization by the NTS may capture the increase in flow strength due to internal hydrogen, the evolution of the stress and strain fields at the notch during fatigue, and/or the effect of hydrogen on the material response. In other words, the fatigue life and notch tensile strength may both be dictated by the evolution of the stress state at the notch and the effect of hydrogen on the deformation processes, which may be similar in tension and fatigue. Although normalization by the UTS has also been shown to collapse the S-N curves for several austenitic stainless steels [8, 9] and the S-N curves for 316L tested with different specimen geometries [12], it is not known whether normalization by the NTS would also collapse fatigue data for different alloys and specimen geometries.

When plotted versus the maximum applied stress, the PC and HP conditions of the 255 DSS and the AR, PC, and HP conditions of the 316L exhibited similar cycles to crack initiation, while the 255 DSS AR exhibited greater cycles to crack initiation (Figure 2 (a)). The 255 DSS AR likely exhibits

greater cycles to crack initiation than the 316L AR because of the higher strength of the 255 DSS; however, the 255 DSS PC and HP conditions and the 316L PC and HP conditions have similar cycles to crack initiation because hydrogen causes a greater decrease in cycles to crack initiation for the 255 DSS than for the 316L. Normalization by the NTS collapsed the 255 DSS data into a single band and the 316L data into a separate band (Figure 2 (b)). These differences in the fatigue behavior for these two alloys is not surprising considering the significant microstructural differences between the fully austenitic 316L and the austenite/ferrite 255 DSS.

The cracks in the AR and PC 255 DSS CNT specimens shown in Figures 3-6 indicate that for both with and without internal hydrogen small cracks likely initiate at and propagate through microstructural stress concentrators. No crack was observed to be entirely contained within one grain and not intersect a phase or grain boundary. The smallest observed cracks in the AR specimen (Figure 3) intersected a γ/α phase boundary and propagated through an austenite island with a diameter less than 10 μm. The shortest crack observed in the PC condition (Figure 5) intersected multiple small austenite islands in a large ferrite grain and exited the ferrite grain at a γ/γ/γ/α quadruple point. Since the austenite is softer in duplex stainless steels than the ferrite, more deformation is likely to occur in the austenite islands, and this may cause the austenite islands themselves to act as microstructural stress concentrators. In fact, Alvarez-Armas, *et al.* has shown that for a DSS tested in the high cycle fatigue regime, deformation mostly occurs in the austenite but not in the ferrite, which leads to crack initiation at γ/α phase boundaries [13]. Magnin, *et al.* have also observed fatigue cracks initiating in austenite in a duplex stainless steel when tested at low strain amplitudes [6].

Grain boundaries and triple points have also been observed to be critical points for crack initiation in 316L both with and without internal hydrogen [11]. Strain incompatibility at triple points and quadruple points in 255 DSS may cause these sites to act as microstructural stress concentrators leading to crack initiation. Phase boundaries and grain boundaries in 255 DSS can be obstacles to dislocation motion resulting in dislocation pile-ups. The pile-up of dislocations at these obstacles would increase the local stress and result in microcrack initiation. The similarity in cracking sites and fatigue crack initiation life for a normalized stress between the 255 DSS AR and PC conditions indicates that hydrogen may not weaken any particular microstructural site. Instead, hydrogen may cause earlier crack initiation for the same absolute stress by enhancing the same crack initiation mechanisms that occur in inert environments,

Cracks were observed to propagate transgranularly through the ferrite and austenite both with and without internal hydrogen. Cracks parallel to slip traces indicate cracking occurring along slip bands. Long transgranular cracks perpendicular to the loading direction and propagating through multiple grains also indicate that cracks may propagate when multiple slip systems are active and the cracking is driven by the normal stress.

Previous analysis of the small crack initiation and propagation sites in strain-hardened 316L with and without internal hydrogen revealed exclusively transgranular cracking, which did not occur along primary slip bands [13]. The differences in microstructural crack path between 255 DSS and 316L indicates that the difference in cycles to crack initiation between the two alloys shown in Figure 2 (b) may be a result of the differences in microstructural sites susceptible to fatigue crack initiation and not exclusively due to differences in mechanical response.

CONCLUSIONS

The influence of internal and external hydrogen on fatigue crack initiation and fatigue life of a 255 super duplex stainless steel was evaluated through fatigue testing of CNT specimens. High pressure hydrogen gas and pre-charged hydrogen similarly decreased the fatigue lives and fatigue limit of 255 duplex stainless steel, but normalization of the applied stress by the notched tensile stress caused the S-N curves for these environments to collapse into a narrow band with the as-received (non-charged) condition. The cycles to crack initiation determined with DCPD exhibited the same trends as cycles to failure for 255 DSS. For both with and without internal hydrogen, small cracks appeared to preferentially intersect phase boundaries, grain boundaries, and other microstructural stress concentrators. No distinct effect of hydrogen on crack path was observed as cracks in specimens with and without internal hydrogen propagated along phase boundaries, grain boundaries, and in a transgranular manner through both the austenite and ferrite.

ACKNOWLEDGEMENTS

The authors gratefully acknowledge assistance from J. McNair and J.A. Campbell for hydrogen pressure systems support. We also acknowledge the funding support of the Energy Efficiency and Renewable Energy Office's Hydrogen and Fuel Cell Technologies Office at the U.S. Department of Energy. Sandia National Laboratories is a multimission laboratory managed and operated by National Technology and Engineering Solutions of Sandia, LLC., a wholly owned subsidiary of Honeywell International, Inc., for the U.S. Department of Energy's National Nuclear Security Administration under contract DE-NA-0003525. This paper describes objective technical results and analysis. Any subjective views or opinions that might be expressed in the paper do not necessarily represent the views of the U.S. Department of Energy or the United States Government.

REFERENCES

[1] C. San Marchi, B. P. Somerday, J. Zelinski, X. Tang, and G. H. Schiroky, "Mechanical properties of super duplex stainless steel 2507 after gas phase thermal precharging with hydrogen," *Metall. Mater. Trans. A Phys. Metall. Mater. Sci.*, vol. 38 A, no. 11, pp. 2763–2775, Nov. 2007.

[2] J. H. Huang and C. J. Altstetter, "Cracking of duplex stainless steel due to dissolved hydrogen," *Metall. Mater. Trans. A*, vol. 26, no. 5, pp. 1079–1085, 1995.

[3] W. Zheng and D. Hardie, “The effect of hydrogen on the fracture of a commercial duplex stainless steel,” *Corros. Sci.*, vol. 32, no. 1, pp. 23–36, 1991.
[4] T. P. Perng and C. J. Altstetter, “Cracking kinetics of two-phase stainless steel alloys in hydrogen gas,” *Metall. Trans. A*, vol. 19, no. 1, pp. 145–152, 1988.
[5] T. J. Marrow, P. J. Cotterill, and J. E. King, “Temperature effects on the mechanism of time independent hydrogen assisted fatigue crack propagation in steels,” *Acta Metall. Mater.*, vol. 40, no. 8, pp. 2059–2068, 1992.
[6] Magnin, T., Lardon, J. M., and Coudreuse, L., "A New Approach to Low Cycle Fatigue Behavior of a Duplex Stainless Steel Based on the Deformation Mechanisms of the Individual Phases," Low Cycle Fatigue, ASTM STP 942. H. D. Solomon, G. R. Halford, L. R. Kaisand, and B. N. Leis, Eds., American Society for Testing and Materials, Philadelphia, 1988, pp. 812-823.
[7] P. J. Gibbs, C. San Marchi, K. A. Nibur, and X. Tang, “Comparison of Internal and External Hydrogen on Fatigue-Life of Austenitic Stainless Steels,” (paper no. PVP2016-63563), in ASME Pressure Vessels and Piping Division Conference, 17-21 July 2016, Vancouver, Canada.
[8] K. A. Nibur, P. J. Gibbs, J. W. Foulk, and C. San Marchi, “Notched Fatigue of Austentic Alloys in Gaseous Hydrogen,” (paper no. PVP2017-65978), in ASME Pressure Vessels and Piping Division Conference, 16-20 July 2017, Waikoloa, Hawaii.
[9] C. San Marchi, P. Gibbs, J. Foulk, and K. A. Nibur, “Fatigue Life of Austenitic Stainless Steel in Hydrogen Environments,” in *43rd MPA Seminar*, 2017.
[10] C. Skipper, G. Leisk, A. Saigal, D. Matson, C. S. Marchi, and C. San Marchi, “Effect of internal hydrogen on fatigue strength of type 316 stainless steel,” in *Proceedings of the 2008 International Hydrogen Conference - Effects of Hydrogen on Materials*, pp. 139–146, 2008.
[11] B. Kagay, J. Ronevich, and C. San Marchi, “Effect of Internal Hydrogen on Fatigue Crack Initiation Sites in 316L Austenitic Stainless Steel,” (paper no. PVP2021-62944), in ASME Pressure Vessels and Piping Division Conference, 2021.
[12] B. Kagay, C. San Marchi, V. Pericoli, and J. Foulk, “Hydrogen effects on fatigue life of welded austenitic stainless steels evaluated with hole-drilled tubular specimens,” (paper no. PVP2020-21288), in ASME Pressure Vessels and Piping Division Conference, 2020.
[13] I. Alvarez-Armas, U. Krupp, M. Balbi, S. Hereñú, M. C. Marinelli, and H. Knobbe, “Growth of short cracks during low and high cycle fatigue in a duplex stainless steel,” *Int. J. Fatigue*, vol. 41, pp. 95–100, Aug. 2012.